Room Temperature Multiferroicity of Charge Transfer Crystals

Wei Qin,[†] Xiaomin Chen,[‡,§] Huashan Li,[∥] Maogang Gong,[†] Guoliang Yuan,[§] Jeffrey C. Grossman,[∥] Manfred Wuttig,[‡] and Shenqiang Ren*[,†]

[†]Department of Mechanical Engineering, Temple University, Philadelphia, Pennsylvania 19122, United States, [‡]Department of Materials Science and Engineering, University of Maryland, College Park, Maryland 20742, United States, [§]School of Materials Science and Engineering, Nanjing University of Science and Technology, Nanjing, China, and [∥]Department of Materials Science and Engineering, Massachusetts Institute of Technology, Cambridge, Massachusetts 02139, United States

ABSTRACT Room temperature multiferroics has been a frontier research field by manipulating spin-driven ferroelectricity or charge-order-driven magnetism. Charge-transfer crystals based on electron donor and acceptor assembly, exhibiting simultaneous spin ordering, are drawing significant interests for the development of all-organic magnetoelectric multiferroics. Here, we report that a remarkable anisotropic magnetization and room temperature multiferroicity can be achieved through assembly of thiophene donor and fullerene acceptor. The crystal motif directs the dimensional and compositional control of charge-transfer networks that could switch magnetization under external stimuli, thereby opening up an attractive class of all-organic nanoferronics.

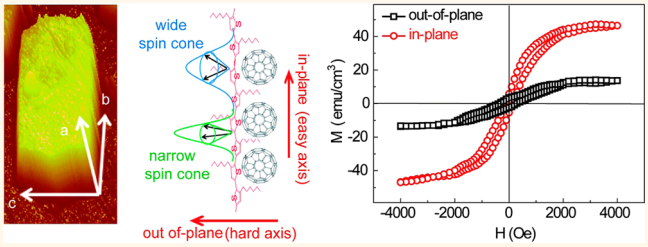

KEYWORDS: organic multiferroics · organic magnetoelectric coupling · organic self-assembly

In the past decade, organic donor and acceptor charge-transfer complexes have been emerged as a fascinating opportunity for the development of all-organic ferroelectrics and spintronics, due to their weak hyperfine interaction and low spin−orbit coupling for organic sensors and energy-efficient memories. The Curie temperatures and switchable polarization of organic ferroelectrics have improved remarkably due to the controlled molecular stacking and a better understanding of organic electronic structures;[1−3] nevertheless, direct observations of room temperature magnetic spin ordering have yet to be accomplished in organic charge-transfer complexes.[4−12] Furthermore, room temperature magnetoelectric coupling effect, hitherto known as multiferroics,[13−22] is anticipated in organic donor−acceptor complexes because of magnetic field dependent charge-transfer dipoles, yet this is also unexplored. A straightforward guideline for designing organic multiferroics might be to use the ordered crystalline networks of electron donors and acceptors, where the collective transfer of electrons from donor to acceptor (or, *vice versa*) results in the formation of simultaneous spin order. In this context, crystal ordering has shown great promise for building three-dimensional donor and acceptor networks to direct noncovalent interactions ($\pi-\pi$ stacking, van der Waals forces and hydrogen-bonding) in a specific direction, which could provide a pathway to guide the development of all-organic magnetoelectric multiferroics due to long-range orientation of spin ordering at ambient temperatures.

RESULTS AND DISCUSSION

Here, we describe three-dimensional assembly of thiophene donor and the well-ordered fullerene acceptor as the prototypical charge-transfer crystals (CTCs). Figure 1a shows three-dimensional atomic force microscope (AFM) image of CTCs based on the thiophene donor and the well-ordered C_{60} acceptor under ambient conditions using acetonitrile (ACN) as the polar solvent (see the Methods section). The overall dimensions of CTCs require a hierarchical organization and long-range noncovalent interactions between the thiophene donor and C_{60} acceptor, where the segregation stacking between the donor and acceptor molecules can be adjusted by the polar solvent loading ratios (Figure 1b). At low polar solvent loading (5 vol %), the weak

* Address correspondence to shenqiang.ren@temple.edu.

Received for review June 11, 2015 and accepted August 8, 2015.

Published online August 08, 2015
10.1021/acsnano.5b03558

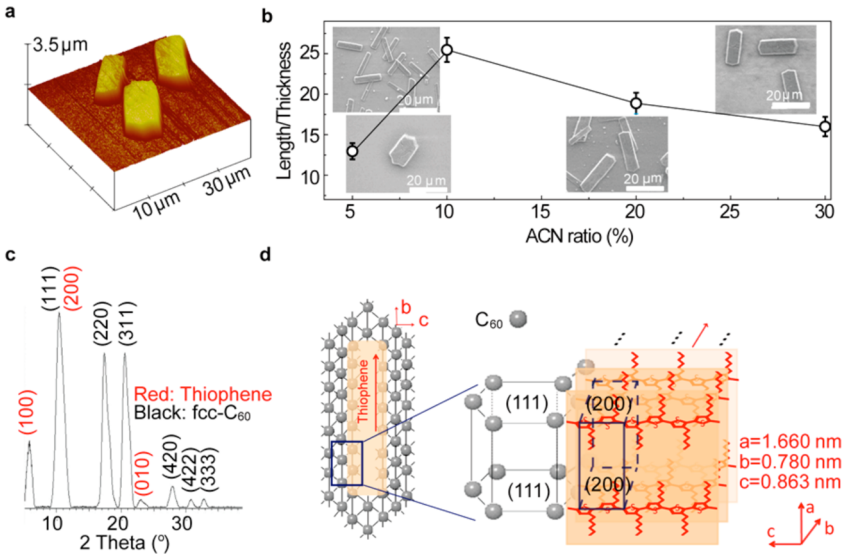

Figure 1. Structure and growth control of CTCs. (a) Three-dimensional atomic force microscope (AFM) image of CTCs. (b) The dimensions and corresponding SEM images of CTCs at 5%, 10%, 20%, and 30% acetonitrile (ACN) polar solvent loading ratios. (c) XRD of SCTCs. (d) The structural schemes and the "close-up" view of SCTCs, respectively.

aggregation induces small density of crystals. However, overloading of the polar solvent (30 vol %), fast aggregation, and stacking of thiophene nanowires tend to yield a small density of crystals with a relatively large dimension. Therefore, an optimum aggregation could enable the formation of molecular assembly achieving high density ribbon-like crystals with a large aspect ratio (Figure S2). An optimum ACN loading (10 vol %) enables high density crystals with an aspect ratio of length/thickness: 26, as shown in Figure 1b. It should be noted that CTCs are only formed when the donor and acceptor are simultaneously ordered[23−25] (Supporting Information, Figure S1). Figure 1c shows X-ray diffraction (XRD) of CTCs, where the *a*-axis is perpendicular to the substrate (the *b*−*c* basal plane).[26] The structural formation of CTCs is facilitated by lattice engineering and molecular packing between the oriented thiophene chains and the well-ordered C_{60} lattices (Figure 1d). The crystallized thiophene donor exhibits the structure with the lattice constant a = 1.660 nm, b = 0.780 nm, and c = 0.863 nm,[26−28] while the well-ordered C_{60} acceptor adopts face-centered cubic (fcc) structure with the lattice constant 1.415 nm.[29−32] The diffraction superimposes to each other between (200)-thiophene and (111)-C_{60} with a lattice mismatch less than 1.57%, meaning that a stable interfacial configuration is formed between (200)-thiophene and (111)-C_{60} structure within the CTCs (Figure 1d). In addition, details of XRD measurements and CIF file are presented in Supporting Information.

The ribbon-like CTCs represent three-dimensional charge-transfer networks, where 10% ACN induced optimum CTCs is selected for the following studies unless otherwise indicated. The resulting crystal structures were characterized by AFM and transmission electron microscopy (TEM). As shown in Figure 2a,d, the CTCs are solid-state structure (more details are shown in Figure S3). During the molecular assembly, the thiophene donor and the well-ordered C_{60} acceptor crystallize as nanoplate units (Figure 2b), which further utilize the structural synergy between noncovalent interactions and charge-transfer complexation to form the ribbon-like CTCs. Figure 2c,f confirms that the nanoplate unit consists of crystallized thiophene nanowires and the well-ordered C_{60} structures, which serve as the building blocks for CTCs. The high-resolution TEM image and selected area electron diffraction (the inset of Figure 2f and Figure S4) confirm the well-ordered fcc C_{60} molecules.[31,32]

Within charge transfer CTCs, by tuning the ratio between singlet and triplet charge-transfer through external stimuli, pronounced magnetic field effects can be observed at room temperature. An external magnetic field (1000 Oe) could readily tune the ratio between singlet and triplet charge-transfer due to small exchange interaction.[33−36] The applied magnetic field could induce less spin mixing, which leads to more triplet charge-transfer[34,35,37,38] to translate into triplet excitons subsequently. The lifetime of singlet excitons is on the order of picoseconds, while the triplet excitons can last for more than microseconds.[39,40] Thus, triplet excitons could contribute to the dipole of CTCs, and an applied magnetic field would increase the ratio of triplet excitons to enhance the dipole density. As shown in Figure 3a, a magnetic field dependent dielectric constant is observed at different frequencies. The magnetic field could enhance the dielectric constant due to the indirect control of triplet exciton density. The dielectric constant tends to saturate when the magnetic field is larger than 500 Oe. The magneto-dielectric effect is defined as $MFD(H) = \{[\varepsilon(H) - \varepsilon(0)]/\varepsilon(0)\}$, where $\varepsilon(H)$ is magnetic field dependent dielectric constant.

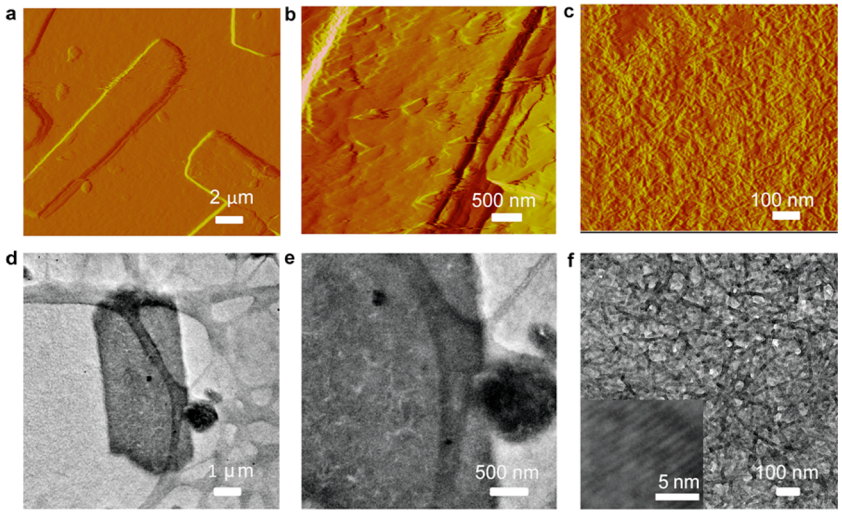

Figure 2. Atomic force microscopy (AFM) and transmission electron microscopy (TEM) images of CTCs at 10% polar solvent loading ratio. (a–c) Low-resolution and high-resolution AFM images of CTCs. (d–f) The corresponding TEM images of CTCs at different resolution, and the inset of (f) shows the high-resolution TEM of the well-ordered C_{60}.

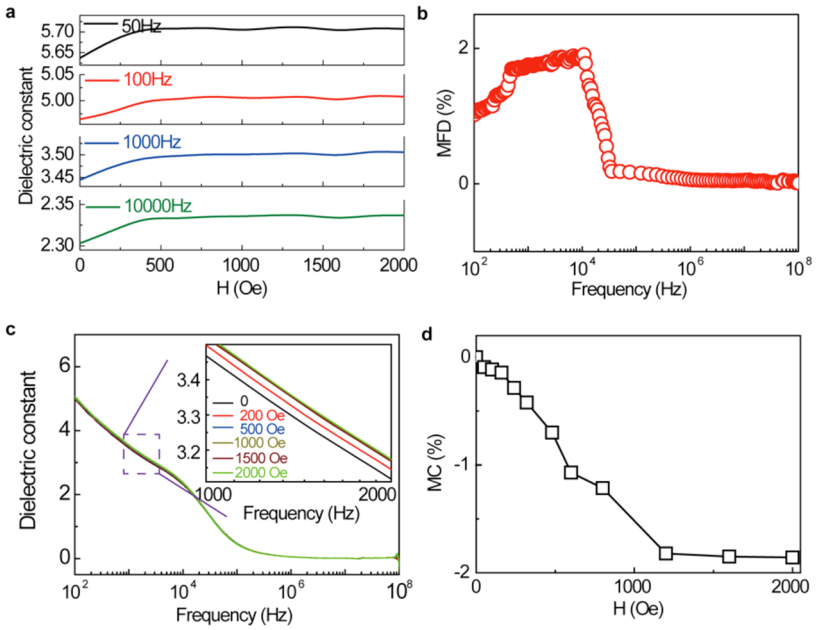

Figure 3. Magnetic field effects on dielectric constant and conductance of CTC devices. (a) Magnetic field dependent dielectric constant at different frequencies. (b) Frequency dependent dielectric constant under the bias 1000 Oe magnetic field. It is noted that dielectric constant can be increased by magnetic field; MFD shows positive signal. (c) Frequency dependent dielectric constant under different external magnetic fields. (d) Tunability of conductance by external magnetic field. Magnetic field can increase the conductance of devices, MC = $[\sigma(B) - \sigma(0)]/\sigma(0)$, where $\sigma(B)$ is the conductance of device under external magnetic field.

It is noted that, by tuning the frequency from 100 to 10000 Hz, MFD increases from 1% to 1.8%, as shown in Figure 3b. The Maxwell–Wagner polarization was widely adopted to explain the high dielectric constant (several hundreds or thousands) observed in the organic or inorganic materials.[41–43] The large dielectric constant resulted from Maxwell–Wagner relaxation occurring at two dielectric media or the interfaces of grains and grain boundaries. In organic charge transfer crystals, dielectric constant is very small with frequency range from 100 Hz to 100 M Hz, as shown in Figure 3c. Therefore, the contribution of Maxwell–Wagner type on dielectric constant is very weak within organic CTCs. As discussed in Figure 3a, magneto-dielectric effect results from spin-dependent transport. To further confirm spin dependent magnetic field effects, magneto-conductance (MC) of CTC devices is studied (MC = $[\sigma(H) - \sigma(0)]/\sigma(0)$, $\sigma(H)$ is the conductance of device under external magnetic field). Due to magnetic field indirectly induced larger density (longer lifetime) spin-tripelt

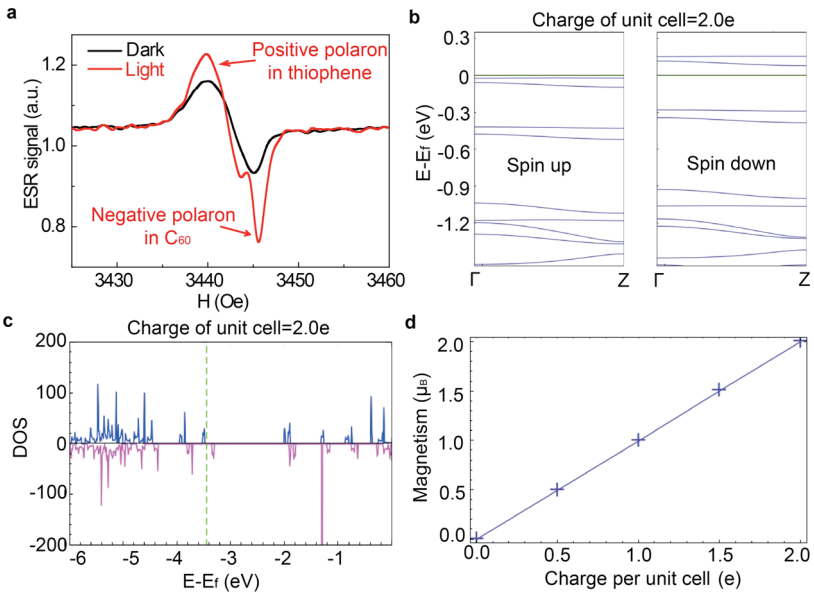

Figure 4. Electron spin resonance (ESR) and magnetic susceptibility of CTCs. (a) ESR signals of CTCs under dark and light environment at 10% polar solvent loading ratio. (b) Energy levels of spin up and spin down with 2 positive charges per unit cell. (c) Density of state with 2 positive charges in CTCs. (d) Charge per unit cell dependent magnetization.

excitons, carriers of CTCs will be scatted by triplet excitons to induce a smaller conductance. Therefore, comparing to positive MFD, negative MC is observed, as shown in Figure 3d.

When a magnetic field and microwave radiation (microwave frequency ν) is applied to the CTCs, electron spin resonance (ESR) could be used to further confirm the existence of charge transfers. Under light excitation, ESR becomes more pronounced, as shown in Figure 4a. It is noted that, due to different g factors of positive and negative polarons, charge transfers can be observed within CTCs (Figure 4a). Within CTCs, charge transfer dependent magnetism was carried out theoretically by the spin unrestricted density functional theory (DFT) framework with the GGA-PBE functionals[44] implemented in the VASP package[45,46] (the molecular structure model is shown in Figure S6). The C_{60} intercalation between the side chains of the thiophene enhances charge-transfer interactions to increase the density of charges in thiophene nanowires.[47] Our results indicate that the observed magnetism likely originates from the charged crystalline thiophene nanowires. The ground state is spin-unpolarized due to the degenerate spin up and spin down energy levels (as shown in Figure S7a,b together with the corresponding wave function in Figure S8). When positive charges are introduced into the thiophene crystal through charge-transfer, the strong coupling from organized π stacking tends to align the spins in the thiophene chain inducing a splitting of energy level between spin up and spin down (Figure 4b), which results in a net magnetic moment as shown in Figure 4c (more details are shown in Figures S7c,d and S8). In addition, it should be noted that the magnetization increases linearly with charges in thiophene lattice due to its flat band structure (Figure 4d, and additional details are shown in the Supporting Information Figure S9).

Experimentally, the magnetic hysteresis loops were employed to elucidate the anisotropy of magnetization within CTCs between in-plane (easy axis) and out-of-plane (hard axis) directions (Figure 5a, and the potential impurity effects were ruled out, as shown in the Supporting Information Figure S12). The charge-lattice coupling within the crystallized thiophene nanowire chain gives rise to the spin density wave leading to the spontaneous magnetization of CTCs. A strong (weak) charge-lattice coupling would induce a narrow (wide) spin cone, which promotes the alignment of spins within the narrow (wide) spin cone along easy (hard) axis (Figure 5b). This orientation dependent magnetic anisotropy leads to a larger magnetization along easy axis, in comparison to the hard axis or the a-axis (Figure 5a).[48] To confirm the orientation and width of spin cone effects on the anisotropy of magnetization, we further investigate its charge density and angular dependence (Figure 5c). As demonstrated, a large length/thickness ratio of CTCs induces high density of charge, leading to a stronger charge-lattice coupling and distortion.[49] This tends to narrow the spin cone along the easy axis for a higher magnetization (widen the spin cone along the hard axis), which broadens the ΔM_s difference (Figure 5c, a large ΔM_s value as increasing the length/thickness ratio). In comparison, a decreased charge density or length/thickness ratio would broaden the spin cone along the hard axis and promote its magnetization, which narrows the ΔM_s difference between the easy axis and

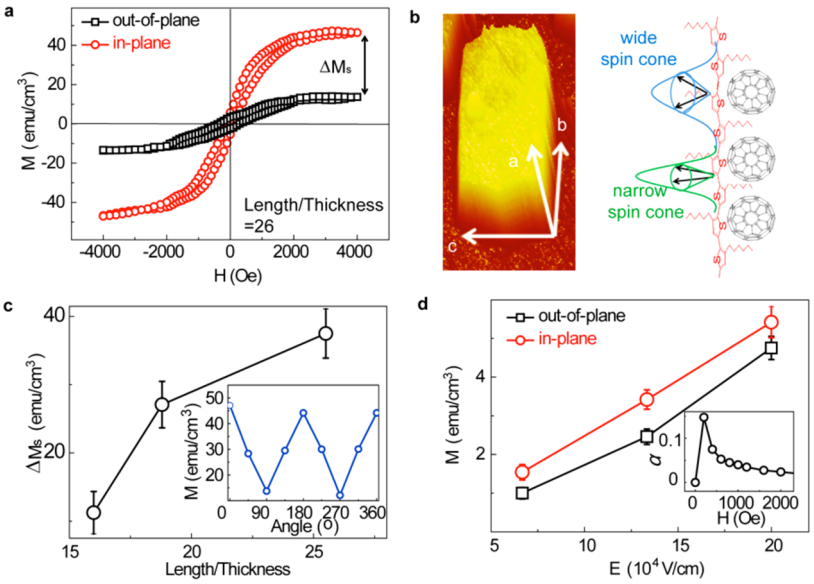

Figure 5. Anisotropy of magnetization and ME coupling in CTCs. (a) The in-plane and out-of-plane magnetic hysteresis (M−H) loops of CTCs. (b) The AFM image of one CTC, and the scheme of spin cone distribution due to the exciton−lattice coupling. The width and orientation of spin cone would be different based on the exciton−lattice coupling extent and spin direction. (c) The length/thickness of CTC dependent anisotropy of magnetization (ΔM_s) between in-plane (easy axis) and out-of-plane (hard axis) directions. The inset shows the angle dependent saturation magnetization M_s (the 0°, 180°, and 360° means magnetic field parallel to in-plane direction). (d) Electric field dependent magnetization (ME coupling) of CTC devices. The inset shows the magnetic field dependent ME coupling coefficient.

hard axis (Figure 5c). Furthermore, when the angle of applied magnetic field is tuned (when magnetic field is parallel to the $b-c$ plane or the easy axis, the angle θ is set as 0° or 180° as shown in the inset of Figure 5c), the saturation magnetization exhibits an angle-dependent behavior between the in-plane (easy axis) and out-of-plane (hard axis) directions, which confirms the angular dependent spin cone orientation effect[50] within the low symmetry of CTCs. Considering the induction of electric polarization by spin current in the spin-current model,[51] we demonstrate room temperature magnetoelectric (ME) coupling effect, as shown in Figure 5d. The tunable polarization by external magnetic field further confirms the ME coupling in CTCs (the inset of Figure 5d) as resulting from the increased triplet exciton density through external magnetic field controlled conversion from singlet to triplet charge-transfer. The optimal ME coupling coefficient $\alpha = 148$ mV cm^{-1} Oe^{1-} ($\Delta E = \alpha \Delta H$) is achieved under 200 Oe bias magnetic field. The ME coupling can be further enhanced by incorporating ferroelectric polymer P(VDF-TrFE) layer, as shown in Figures S14 and S15.

CONCLUSIONS

In summary, three-dimensional CTCs, consisting of the well-ordered fullerene acceptor and crystallized thiophene nanowire donor, has been designed. The spin order arise simultaneously, accompanied by external-stimuli controlled magnetoelectric coupling, thus leading to room temperature multiferroicity in this material. DFT provides the insight into the charge-driven magnetism and unusual temperature-dependent magnetic susceptibilities. The anisotropic magnetization of CTCs can be ascribed to the strong exciton-lattice coupling induced by molecule assembly and the orientation of spin cone.

METHODS

Synthesis of Molecular Charge-Transfer Crystals. First, polythiophene was dissolved by 1,2-dichlorobenzene (1,2-DCB) (20 mg/mL), and the C_{60} was added into the polythiophene solution at the weight ratio 1:1. After 10 h stirring, polar solvent was added into the mixed solution (adding 5−30 vol % polar solvent) at room temperature, followed by a low power ultrasonic agitation (5 min). The solution was aged for 2 days before the usage. After spin coating solution on Si substrates, the size (average of 50 CTCs with the same polar solvent loading ratio) of each type CTC was studied by AFM.

Device Structure. Indium tin oxide (ITO) was chosen as the bottom electrode. After cleaning, ITO substrates were coated with poly(3,4-ethylenedioxythiophene)/polystyrenesulfonate (PEDOT/PSS) by spin coating at 3800 rpm for 1 min. Then, molecular crystal layer was applied by spin coating at 2000 rpm for 1 min. Aluminum electrodes were deposited on the devices through thermal evaporation, defining a device area of 0.65 × 1.75 mm^2

ESR Measurements. Bruker EMX (type: ER073) plus ESR spectrometer is used to measure ESR signal. After 10 h of continuous stirring, solution (150 μL) was injected into a glass tube in a nitrogen-filled glovebox. Each ESR signal was measured as the average of 10 sweeps.

Magnetic Hysteresis (M-H) Loop Measurements. A MicroSense EV7 vibrating sample magnetometer (VSM) was used to measure M-H loops of all thin film and powder samples. ITO (Al) was connected as an anode (cathode) for the measurement of electric field dependent magnetization.

Atomic Absorption Measurement. A SpectrAA 220FS (Varian, Inc.) atomic absorption spectrophotometer was adopted to measure the concentrations of Fe and Ni in CTCs. Each atomic absorption signal was measured as the average of 3 sweeps.

Dielectric Constant. The dielectric constant measurements were performed with Agilent 4294a Precision impedance with a frequency range from 40 Hz to 110 MHz at a constant bias of 100 mV.

DFT Calculation Details. Standard *ab initio* calculations were performed with the Vienna Ab Initio Simulation Package (VASP).[46] Plane wave and projector augmented wave (PAW) type pseudopotentials[45] with kinetic energy cutoffs of up to 500 eV were applied, using a Monkhorst–Pack grid[52] with 19 k points sampling along the axis of nanowire. The structures were relaxed until all forces were smaller than 0.03 eV/A. The simplification of the molecule structure is justified by a control calculation on P3MT crystal with shorter side chains.

Conflict of Interest: The authors declare no competing financial interest.

Acknowledgment. S.R thanks the Army Research Office - Young Investigator Program (W911NF-14-1-0443, material design/self-assembly of carbon magnetoelectrics) and Department of Energy-Basic Energy Sciences Award No. DE-FG02-13ER46937 (organic synthesis and physical property measurement), and M.W. thanks the financial support from U.S. Department of Energy (DOE DESC0005448).

Supporting Information Available: The Supporting Information is available free of charge on the ACS Publications website at DOI: 10.1021/acsnano.5b03558.

Description of particles XRD and ESR measurements and calculation details (PDF)

Crystallographic data for thiophene and C_{60} structure within the CTCs (CIF)

REFERENCES AND NOTES

1. Horiuchi, S.; Tokunaga, Y.; Giovannetti, G.; Picozzi, S.; Itoh, H.; Shimano, R.; Kumai, R.; Tokura, Y. Above-Room-Temperature Ferroelectricity in a Single-Component Molecular Crystal. *Nature* **2010**, *463*, 789–792.
2. Tayi, A. S.; Shveyd, A. K.; Sue, A. C. H.; Szarko, J. M.; Rolczynski, B. S.; Cao, D.; Kennedy, T. J.; Sarjeant, A. A.; Stern, C. L.; Paxton, W. F.; et al. Room-Temperature Ferroelectricity in Supramolecular Networks of Charge-Transfer Complexes. *Nature* **2012**, *488*, 485–489.
3. Fu, D. W.; Cai, H. L.; Liu, Y.; Ye, Q.; Zhang, W.; Zhang, Y.; Chen, X. Y.; Giovannetti, G.; Capone, M.; Li, J.; et al. Diisopropylammonium Bromide Is a High-Temperature Molecular Ferroelectric Crystal. *Science* **2013**, *339*, 425–428.
4. Mihailovic, D.; Arcon, D.; Venturini, P.; Blinc, R.; Omerzu, A.; Cevc, P. Orientational and Magnetic Ordering of Buckyballs in TDAE-C_{60}. *Science* **1995**, *268*, 400–402.
5. Narymbetov, B.; Omerzu, A.; Kabanov, V. V.; Tokumoto, M.; Kobayashi, H.; Mihailovic, D. Origin of Ferromagnetic Exchange Interactions in a Fullerene-Organic Compound. *Nature* **2000**, *407*, 883–885.
6. Mizoguchi, K.; Machino, M.; Sakamoto, H.; Kawamoto, T.; Tokumoto, M.; Omerzu, A.; Mihailovic, D. Pressure effect in TDAE-C_{60} ferromagnet: Mechanism and polymerization. *Phys. Rev. B: Condens. Matter Mater. Phys.* **2001**, *63*, 140417.
7. Stephens, P. W.; Cox, D.; Lauher, J. W.; Mihaly, L.; Wiley, J. B.; Allemand, P. M.; Hirsch, A.; Holczer, K.; Li, Q.; Thompson, J. D.; et al. Lattice Structure of the Fullerene Ferromagnet TDAE-C_{60}. *Nature* **1992**, *355*, 331–332.
8. Deligiannakis, Y.; Papavassiliou, G.; Fardis, M.; Diamantopoulos, G.; Milia, F.; Christides, C.; Pokhodnia, K. I.; Barchuk, V. Direct Observation of Electron Spin Density on TDAE Cations in the Ferromagnetic State of Solid TDAE-C_{60}. *Phys. Rev. Lett.* **1999**, *83*, 1435–1438.
9. Kagawa, F.; Horiuchi, S.; Tokunaga, M.; Fujioka, J.; Tokura, Y. Ferroelectricity in a One-Dimensional Organic Quantum Magnet. *Nat. Phys.* **2010**, *6*, 169–172.
10. Miyamoto, T.; Yada, H.; Yamakawa, H.; Okamoto, H. Ultrafast Modulation of Polarization Amplitude by Terahertz Fields in Electronic-Type Organic Ferroelectrics. *Nat. Commun.* **2013**, *4*, 2586.
11. Lunkenheimer, P.; Müller, J.; Krohns, S.; Schrettle, F.; Loidl, A.; Hartmann, B.; Rommel, R.; Souza, M.; Hotta, C.; Schlueter, J. A.; et al. Multiferroicity in an Organic Charge-Transfer Salt That Is Suggestive of Electric-Dipole-Driven Magnetism. *Nat. Mater.* **2012**, *11*, 755–758.
12. Qin, W.; Gong, M.; Chen, X.; Shastry, T. A.; Sakidja, R.; Yuan, G.; Hersam, M. C.; Wuttig, M.; Ren, S. Multiferroicity of Carbon-Based Charge-Transfer Magnets. *Adv. Mater.* **2015**, *27*, 734–739.
13. Zavaliche, F.; Zhao, T.; Zheng, H.; Straub, F.; Cruz, M. P.; Yang, P. L.; Hao, D.; Ramesh, R. Electrically Assisted Magnetic Recording in Multiferroic Nanostructures. *Nano Lett.* **2007**, *7*, 1586–1590.
14. Scott, J. F. Data Storage: Multiferroic Memories. *Nat. Mater.* **2007**, *6*, 256–257.
15. Hur, N.; Park, S.; Sharma, P. A.; Ahn, J. S.; Guha, S.; Cheong, S. W. Electric Polarization Reversal and Memory in a Multiferroic Material Induced by Magnetic Fields. *Nature* **2004**, *429*, 392–395.
16. Lage, E.; Kirchhof, C.; Hrkac, V.; Kienle, L.; Jahns, R.; Knöchel, R.; Quandt, E.; Meyners, D. Exchange Biasing of Magnetoelectric Composites. *Nat. Mater.* **2012**, *11*, 523–529.
17. Cheong, S. W.; Mostovoy, M. Multiferroics: a Magnetic Twist for Ferroelectricity. *Nat. Mater.* **2007**, *6*, 13–20.
18. Wang, Y.; Hu, J.; Lin, Y.; Nan, C. W. Multiferroic Magnetoelectric Composite Nanostructures. *NPG Asia Mater.* **2010**, *2*, 61–68.
19. Chu, Y. H.; Martin, L. W.; Holcomb, M. B.; Gajek, M.; Han, S. J.; He, Q.; Balke, N.; Yang, C. H.; Lee, D.; Hu, W.; et al. Electric-Field Control of Local Ferromagnetism Using a Magnetoelectric Multiferroic. *Nat. Mater.* **2008**, *7*, 478–482.
20. Wu, S. M.; Cybart, S. A.; Yu, P.; Rossell, M. D.; Zhang, J. X.; Ramesh, R.; Dynes, R. C. Reversible Electric Control of Exchange Bias in a Multiferroic Field-Effect Device. *Nat. Mater.* **2010**, *9*, 756–761.
21. Ramesh, R.; Spaldin, N. A. Multiferroics: Progress and Prospects in Thin Films. *Nat. Mater.* **2007**, *6*, 21–29.
22. Qin, W.; Xu, B.; Ren, S. An Organic Approach for Nanostructured Multiferroics. *Nanoscale* **2015**, *7*, 9122–9132.
23. Ren, S.; Wuttig, M. Organic Exciton Multiferroics. *Adv. Mater.* **2012**, *24*, 724–727.
24. Qin, W.; Lohrman, J.; Ren, S. Magnetic and Optoelectronic Properties of Gold Nanocluster–Thiophene Assembly. *Angew. Chem., Int. Ed.* **2014**, *53*, 7316–7319.
25. Qin, W.; Jasion, D.; Chen, X.; Wuttig, M.; Ren, S. Charge-Transfer Magnetoelectrics of Polymeric Multiferroics. *ACS Nano* **2014**, *8*, 3671–3677.
26. Aryal, M.; Trivedi, K.; Hu, W. Nano-Confinement Induced Chain Alignment in Ordered P3HT Nanostructures Defined by Nanoimprint Lithography. *ACS Nano* **2009**, *3*, 3085–3090.
27. Kim, D. H.; Han, J. T.; Park, Y. D.; Jang, Y.; Cho, J. H.; Hwang, M.; Cho, K. Single-Crystal Polythiophene Microwires Grown by Self-Assembly. *Adv. Mater.* **2006**, *18*, 719–723.
28. Park, Y. D.; Lee, H. S.; Choi, Y. J.; Kwak, D.; Cho, J. H.; Lee, S.; Cho, K. Solubility-Induced Ordered Polythiophene Precursors for High-Performance Organic Thin-Film Transistors. *Adv. Funct. Mater.* **2009**, *19*, 1200–1206.
29. Heiney, P. A.; Fischer, J. E.; McGhie, A. R.; Romanow, W. J.; Denenstein, A. M.; McCauley, J. P.; Smith, A. B.; Cox, D. E. Orientational ordering transition in solid C_{60}. *Phys. Rev. Lett.* **1991**, *66*, 2911–2914.
30. Sathish, M.; Miyazawa, K. i.; Hill, J. P.; Ariga, K. Solvent Engineering for Shape-Shifter Pure Fullerene (C_{60}). *J. Am. Chem. Soc.* **2009**, *131*, 6372–6373.
31. Wang, L.; Liu, B.; Liu, D.; Yao, M.; Hou, Y.; Yu, S.; Cui, T.; Li, D.; Zou, G.; Iwasiewicz, A.; et al. Synthesis of Thin, Rectangular C_{60} Nanorods Using m-Xylene as a Shape Controller. *Adv. Mater.* **2006**, *18*, 1883–1888.
32. Ji, H. X.; Hu, J. S.; Wan, L. J.; Tang, Q. X.; Hu, W. P. Controllable Crystalline Structure of Fullerene Nanorods and Transport

Properties of an Individual Nanorod. *J. Mater. Chem.* **2008**, *18*, 328–332.
33. Hu, B.; Wu, Y. Tuning Magnetoresistance between Positive and Negative Values in Organic Semiconductors. *Nat. Mater.* **2007**, *6*, 985–991.
34. Qin, W.; Gao, K.; Yin, S.; Xie, S. J. Investigating the Magnetic Field Effect on Electron-Hole Pair in Organic Semiconductor Devices. *J. Appl. Phys.* **2013**, *113*, 193901.
35. Janssen, P.; Cox, M.; Wouters, S. H. W.; Kemerink, M.; Wienk, M. M.; Koopmans, B. Tuning Organic Magnetoresistance in Polymer-Fullerene Blends by Controlling Spin Reaction Pathways. *Nat. Commun.* **2013**, *4*, 2286.
36. Majumdar, S.; Majumdar, H. S.; Aarnio, H.; Vanderzande, D.; Laiho, R.; Österbacka, R. Role of Electron-Hole Pair Formation in Organic Magnetoresistance. *Phys. Rev. B: Condens. Matter Mater. Phys.* **2009**, *79*, 201202.
37. Qin, W.; Gong, M.; Shastry, T.; Hersam, M.; Ren, S. Charge-Transfer Induced Magnetic Field Effects of Nano-Carbon Heterojunctions. *Sci. Rep.* **2014**, *4*, 6126.
38. Qin, W.; Yin, S.; Gao, K.; Xie, S. J. Investigation on Organic Magnetoconductance Based on Polaron-Bipolaron Transition. *Appl. Phys. Lett.* **2012**, *100*, 233304.
39. Baldo, M. A.; O'Brien, D. F.; You, Y.; Shoustikov, A.; Sibley, S.; Thompson, M. E.; Forrest, S. R. Highly Efficient Phosphorescent Emission from Organic Electroluminescent Devices. *Nature* **1998**, *395*, 151–154.
40. Jariwala, D.; Sangwan, V. K.; Lauhon, L. J.; Marks, T. J.; Hersam, M. C. Carbon nanomaterials for electronics, optoelectronics, photovoltaics, and sensing. *Chem. Soc. Rev.* **2013**, *42*, 2824–2860.
41. Li, W.; Auciello, O.; Premnath, R. N.; Kabius, B. Giant Dielectric Constant Dominated by Maxwell−Wagner Relaxation in Al_2O_3/TiO_2 Nanolaminates Synthesized by Atomic Layer Deposition. *Appl. Phys. Lett.* **2010**, *96*, 162907.
42. Liu, J.; Duan, C. G.; Yin, W. G.; Mei, W. N.; Smith, R. W.; Hardy, J. R. Large Dielectric Constant and Maxwell-Wagner Relaxation in BCTO. *Phys. Rev. B: Condens. Matter Mater. Phys.* **2004**, *70*, 144106.
43. Catalan, G. Magnetocapacitance without Magnetoelectric Coupling. *Appl. Phys. Lett.* **2006**, *88*, 102902.
44. Perdew, J. P.; Burke, K.; Ernzerhof, M. Generalized Gradient Approximation Made Simple. *Phys. Rev. Lett.* **1996**, *77*, 3865–3868.
45. Blöchl, P. E. Projector Augmented-Wave Method. *Phys. Rev. B: Condens. Matter Mater. Phys.* **1994**, *50*, 17953–17979.
46. Kresse, G.; Furthmüller, J. Efficient Iterative Schemes for *ab initio* Total-Energy Calculations Using a Plane-Wave Basis Set. *Phys. Rev. B: Condens. Matter Mater. Phys.* **1996**, *54*, 11169–11186.
47. Miller, N. C.; Sweetnam, S.; Hoke, E. T.; Gysel, R.; Miller, C. E.; Bartelt, J. A.; Xie, X.; Toney, M. F.; McGehee, M. D. Molecular Packing and Solar Cell Performance in Blends of Polymers with a Bisadduct Fullerene. *Nano Lett.* **2012**, *12*, 1566–1570.
48. Armstrong, J. N.; Hua, S. Z.; Chopra, H. D. Anisotropic Curie Temperature Materials. *Phys. Status Solidi B* **2013**, *250*, 387–395.
49. Gao, K.; Xie, S.; Yin, S.; Liu, D. Biexcitons Generation in a Polymer by a Femtosecond Electric Pump Pulse. *Org. Electron.* **2012**, *13*, 784–788.
50. Callen, E. R. Anisotropic Magnetization. *J. Appl. Phys.* **1960**, *31*, S149–S150.
51. Katsura, H.; Nagaosa, N.; Balatsky, A. V. Spin Current and Magnetoelectric Effect in Noncollinear Magnets. *Phys. Rev. Lett.* **2005**, *95*, 057205.
52. Monkhorst, H. J.; Pack, J. D. Special Points for Brillouin-Zone Integrations. *Phys. Rev. B* **1976**, *13*, 5188–5192.